Manuscript

**Submission as TECHNICAL NOTE to *Medical Engineering & Physics***

# A Comprehensive Three-Dimensional Dynamic Model of the Human Head and Trunk for Estimating Lumbar and Cervical Joint Torques and Forces From Upper Body Kinematics

Running Head: A Comprehensive Three-Dimensional Dynamic Model of the Human Head and Trunk


Authors:

Albert H. Vette[1,2], Takashi Yoshida[1,2], T. Adam Thrasher[3], K. Masani[2], and Milos R. Popovic[1,2]

Affiliations:

[1] Institute of Biomaterials and Biomedical Engineering, University of Toronto, 164 College Street, Toronto, Ontario, M5S 3G9, Canada

[2] Lyndhurst Centre, Toronto Rehabilitation Institute, 520 Sutherland Drive, Toronto, Ontario, M4G 3V9, Canada

[3] Center for Neuromotor and Biomechanics Research, University of Houston, 2450 Holcombe Boulevard, Houston, Texas 77021, USA


November 15, 2011

Number of words in Text: **5,559**

Number of words in Abstract: **248**


Corresponding Author:

Albert H. Vette, Ph.D.
506 ½ Clinton Street
Toronto, Ontario
M6G 2Z4, Canada
Phone: +1-416-964-7145
Email: ahvette@uwaterloo.ca

**ABSTRACT**

Linked-segment representations of human body dynamics have been used extensively in biomechanics, ergonomics, and rehabilitation research to systemize thinking, make predictions, and suggest novel experiments. In the scope of upper body biomechanics, these models play an even more essential role as the human spine dynamics are difficult to study *in vivo*. No study exists to date, however, that specifically disseminates the technical details of a comprehensive three-dimensional model of the upper body for the purpose of estimating spinal joint torques and forces for a wide range of scenarios. Consequently, researchers are still bound to develop and implement their own models. Therefore, the objective of this study was to design a dynamic model of the upper body that can comprehensively estimate spinal joint torques and forces from upper body kinematics. The proposed three-dimensional model focuses on the actions of the lumbar and cervical vertebrae and consists of five lumbar segments (L1 to L5), the thorax, six cervical segments (C2 to C7), and the head. Additionally, the model: (1) is flexible regarding the kinematic nature of the spinal joints (free, constrained, or fixed); (2) incorporates all geometric and mass-inertia parameters from a single, high-resolution source; and (3) can be feasibly implemented via different inverse dynamics formulations. To demonstrate its practicality, the model was finally employed to estimate the lumbar and cervical joint torques during perturbed sitting using experimental motion data. Considering the growing importance of mathematical predictions, the developed model should become an important resource for researchers in different fields.

**INDEX TERMS** – Biomechanics, body kinematics, dynamic modeling, head, inverse dynamics, joint forces, joint torques, spine, trunk, upper body.

## 1. INTRODUCTION

Linked-segment representations of the human body have been used extensively in biomechanics, ergonomics, and rehabilitation research to systemize thinking, make predictions, and suggest novel experiments [1]. In fact, *bimodal* approaches that combine biomechanical modeling with experimental data to investigate newly emerging research questions have become the preferred scientific method (e.g., [2-6]). This can be explained by the belief that such approaches may lead to a better understanding of how the central nervous system and the musculoskeletal system interact to produce movement or maintain postural stability [7]. Due to the ever-increasing performance of computers, especially the use of *dynamic* linked-segment models in studying movement continues to grow: Today, large-scale models of the body can be implemented in simulations that are an order of magnitude more complex than just ten years ago [7-9].

In the particular scope of head and trunk biomechanics, linked-segment models play an even more essential role as the dynamics of the spine are difficult to study *in vivo* compared to most other structures of the human body. Technical difficulties either preclude direct, yet non-invasive measurement and verification of parameters (such as joint torques) or make experiments very time consuming, cumbersome, and error prone [1,10]. In addition, considering the unique structure and usage of the human spine, it is undesirable to resort to animal models [11]. Consequently, mathematical modeling techniques are crucial for studying the dynamics of the upper body and to estimate joint torques and constraint forces for a wide range of scenarios. Note that the classical method of determining these quantities from body kinematics is termed *inverse dynamics* [3,7,10].

Initial interest in mathematical modeling of the upper body arose in the context of studying pilot ejection procedures [12,13]. More recently, linked-segment models of the upper body have been employed to investigate the intrinsic stability of the spine [14-16], the kinetics of vertebral trunk segments during various tasks [2,4,11,17-22], or the coordination and control of head-trunk dynamics during external perturbations [23-25]. Besides these fundamental efforts, more clinically focused studies have relied on linked-segment models to predict spinal or head injuries caused by sudden seat displacements [26-28], to characterize the biomechanics of low back disorders [29,30], or to evaluate the feasibility of controlling seated posture after spinal cord injury via functional electrical stimulation [5,31,32].

In spite of these manifold model applications, no study has disseminated the technical details of a comprehensive three-dimensional model of the upper body. As a result, researchers are still bound to develop and implement their own models of the upper body. At the same time, the use of a standardized dynamic model of the upper body would allow for the validation of results across different studies and research groups. Therefore, the objective of this study was to design a three-dimensional dynamic model of the upper body that can comprehensively estimate spinal joint torques and forces from upper body kinematics. In this context, it has to be emphasized that the identified spinal joint torques and forces are bundled representations of the forces and torques generated via different mechanisms such as muscle activation [33,34], soft tissue and spine stiffness [35-38], and intra-abdominal pressure [38,39].

Specific requirements of the developed model were that it: (1) is flexible regarding the kinematic nature of the spinal joints (free, constrained, or fixed); (2) incorporates all geometric and mass-inertia parameters from a single, high-resolution source; and (3) can be feasibly implemented via different inverse dynamics formulations. To demonstrate its practicality, the model finally predicted the lumbar and cervical joint torques during perturbed sitting using experimental motion data.

# 2. MODELING

## 2.1. Geometric Modeling

The proposed geometric model of the upper body focuses on the actions of the lumbar and cervical vertebrae, which are responsible for the majority of the spine and head movement. The thoracic spine on the other hand was assumed to be rigid based on the report that the vertebral thorax segments (as linked to vertebrae T1 to T12) exhibit less relative movement during trunk motion [40]. As shown in Fig. 1, the model consisted of thirteen rigid bodies, representing five lumbar segments (L1 to L5), the thorax (TH), six cervical segments (C2 to C7), and the head portion adjacent to the C2 segment (HD). The lowest moving segment, i.e., the L5 segment, was located above the pelvis (PV), which marked the inertial frame of reference $\{F_{WD}\}$ ($X_{WD}$: superior; $Y_{WD}$: anterior; $Z_{WD}$: left). For the purpose of the model application in Section 3, the inertial properties of the arms were incorporated into TH (Fig. 1).

To accurately model upper body motion in three-dimensional space, the thirteen rigid bodies were separated from each other by three-dimensional revolute joints that were located at respective centers of thirteen intervertebral discs. The two joints between the cervical and thoracic spine (C7-TH) and between the lumbar spine and the pelvis (L5-PV) had three degrees of freedom (DOF) each (see Fig. 1), consisting of flexion-extension (FE), lateral bending (LB), and axial rotation (RT). The remaining six cervical (HD-C2 to C6-C7) and five lumbar (TH-L1 to L4-L5) joints were treated as revolute constraints (CT; see Fig. 1) with respect to the three-dimensional motion of the 'DOF-joints' C7-TH and L5-PV, respectively. Note that a particular CT's rotation was defined as a fraction of the rotation of the subjacent DOF-joint based on the two joints' ranges of motion as reported by White and Panjabi [35]. In other words, any change in thorax angle (head angle) was distributed across the lumbar (cervical) joints based on the joints' functional ranges of motion. The constraint equations for all CT and all directions of motion are listed in Table 1.

## 2.2. Kinematic Modeling

In order to identify the dynamic model and apply the inverse dynamics method, the kinematics of each model segment had to be described in local frames of reference ($\{F_{SEG}\}$). The frame assignment of the model, which is shown in Fig. 2, followed the Standard Denavit-Hartenberg notation [41] as it elegantly describes the kinematic relationship between the joint variables of the model. The required parameters consisted of the constant link lengths $a_i$, the constant link offsets $d_i$, the constant twist angles $\alpha_i$, and the time-varying revolute joint angles $q_i$. The quantities $a_i$ and $d_i$ represent the vertical and horizontal distances between the centers of the intervertebral discs, respectively, and were taken from the *Male Visible Human* (age: 38 years; height: 1.80 m; weight: 90 kg) as reported in our previous study [42]. The last frame $\{F_{39}\}$ was assigned to the vertex of the head, whereas the inertial coordinate frame $\{F_0\}$ represented a fixed translation of the world frame $\{F_{WD}\}$ to the L5-PV joint. All link parameters are listed in Table 2.

Due to the fact that the frame assignment was selected to yield a constant twist angle ($\alpha_i$) of 90 degrees for all frames, the transformation matrix from frame *i-1* to *i* ($T_{i-1,i}$) was given by:

$$T_{i-1,i} = \begin{bmatrix} \cos q_i & 0 & \sin q_i & a_i \cos q_i \\ \sin q_i & 0 & -\cos q_i & a_i \sin q_i \\ 0 & 1 & 0 & d_i \\ 0 & 0 & 0 & 1 \end{bmatrix} \tag{1}$$

This property simplified the implementation of the kinematic and dynamic models.

### 2.3. Inverse Dynamics

To allow different constraint selections for the kinematic model shown in Fig. 2, all CT of the dynamic model were treated as DOF (thirteen joints with three DOF each). The model's equation of motion was derived symbolically following the method proposed by Kim [43]:

$$\tau = M(q)\ddot{q} + C(q,\dot{q})\dot{q} + G(q) - {}^{0}J^{T}\ {}^{0}F_{ext}, \tag{2}$$

where $\tau \in \Re^{39\times 1}$ is the joint torque, and $q, \dot{q}, \ddot{q} \in \Re^{39\times 1}$ are the joint angle, velocity, and acceleration, respectively. $M(q) \in \Re^{39\times 39}$ is the inertia matrix, $C(q,\dot{q}) \in \Re^{39\times 39}$ the Coriolis-centrifugal matrix, $G(q) \in \Re^{39\times 1}$ the gravity vector, ${}^{0}J^{T} \in \Re^{39\times 6}$ the transpose of the Jacobian matrix with respect to the base frame $\{F_0\}$, and ${}^{0}F_{ext} \in \Re^{6\times 1}$ the external generalized force expressed in the base frame $\{F_0\}$.

To calculate the spinal joint torques for upper body motion, the inverse dynamics of the model were implemented via (1) the Newton-Euler formulation, (2) the Lagrangian formulation (both in Matlab, The MathWorks, USA), and (3) a block diagram within a commercial simulation environment (Simulink & SimMechanics, The MathWorks, USA). Considering that experimental torque data from the spine are not easily available, using three different methods allowed us to ensure the internal validity of the results. The three inverse dynamics formulations (see *Appendix A* for implementation details) had the following commonalities:

(1) three DOF per joint were implemented using a series of links with zero mass and zero length [44];

(2) time derivatives of joint angles were obtained using the central difference scheme [45]; and

(3) the required mass-inertia characteristics were taken from the *Male Visible Human* [42].

# 3. APPLICATION: PERTURBED SITTING

To demonstrate the practicality of the developed model, the inverse dynamics routines were used to predict the lumbar and cervical joint torques of one subject during perturbed sitting. In this context, an inverse kinematics model had to be identified to transform the experimental motion data into joint angles as needed in the inverse dynamics calculations. Finally, a singularity analysis has been included in Appendix B for the benefit of implementing the dynamic model in closed-loop control schemes.

## 3.1. Subject and Experimental Procedure

The healthy male subject was 34 years of age, had very similar anthropometrics as the Male Visible Human (height: 1.80 m; weight: 89 kg), and reported no history of neuromuscular disorders or chronic back pain. He gave written informed consent to the experimental procedure, which was approved by the ethics committees of the University of Toronto and the Toronto Rehabilitation Institute in accordance with the declaration of Helsinki on the use of human subjects in experiments.

Complete details on the experimental procedure have been reported elsewhere [33,34]. In agreement with different recommendations on motion data acquisition [46-48], two sets of four non-collinear markers were mounted on lightweight rigid panels and attached to the back of the subject's TH and HD. To rule out pelvic movement [34], four additional markers were attached on top of the left and right posterior pelvis. The subject was instructed to cross his arms lightly, close his eyes, and sit in a relaxed and natural upright posture. A total of 40 perturbation trials (eight horizontal directions, five trials each) were applied to the subject. Perturbations were delivered in the following directions, relative to the sagittal axis: 0º (anterior), 45º, 90º (right), 135º, 180º (posterior), 225º, 270º (left), and 315º. The order of the perturbation directions was randomized to prevent anticipation, which has a significant effect on the perturbation response [49]. The horizontal perturbation had a Gaussian profile, a peak of approximately 200 N, and was applied just inferior to the axillae (T7 segment). The force and motion data, which are the required inputs for the inverse dynamics routine, were captured at 100 Hz using a load cell (MLP-100-CO-C, Transducer Techniques, USA) and an Optotrak 3020 motion analysis system (Northern Digital Inc., Canada), respectively.

### 3.2. Inverse Kinematics Model

In order to estimate the joint torques via the inverse dynamics method, the time-varying joint angles have to be extracted from the experimentally identified body kinematics. In classical robotics, *inverse kinematics* determine the values of the joint angles for a given robot configuration that places the *end-effector* at a particular position and orientation relative to the base. In the biomechanical context it is common, however, to avoid multiple solutions by capturing the position and orientation of *multiple* body segments. We therefore identified an inverse kinematics model that estimated the joint angles from the TH and HD orientations.

Following the experiments, the three-dimensional data points of the Optotrak markers were used to determine a set of orthogonal unit coordinates defining the time-varying rotation matrix of a given segment's local coordinate frame {$F_{SEG}$} with respect to the world frame {$F_{WD}$}, called $R_{WD\_SEG}$ [50,51]. After calibrating the rotation matrices $R_{WD\_TH}(t)$ and $R_{WD\_HD}(t)$ against the upright sitting posture using the technique described by Areblad et al. [52], the three-dimensional rotation angles were computed as follows:

$$\begin{aligned}
\beta &= \angle Y_{WD}\,(LB) = {}^{2}\tan^{-1}(-r_{31}, \sqrt{r_{11}^2 + r_{21}^2}) \\
\alpha &= \angle X_{WD}\,(RT) = {}^{2}\tan^{-1}(r_{32}/\cos\beta,\ r_{33}/\cos\beta)\,, \\
\gamma &= \angle Z_{WD}\,(FE) = {}^{2}\tan^{-1}(r_{21}/\cos\beta,\ r_{11}/\cos\beta)
\end{aligned} \tag{3}$$

where $^2tan^{-1}$ computes $tan^{-1}(y/x)$, but uses the signs of both $x$ and $y$ to determine the quadrant in which the resulting angle lies. Note that Eq. (3) results from the Cardan rotation sequence RT-LB-FE (yaw, roll, and pitch) about the fixed axes of $\{F_{WD}\}$ – or FE-LB-RT (pitch, roll, and yaw) about the moving axes of $\{F_{SEG}\}$ – which is the preferred order for calculating human joint angles in general [53] and spinal joint angles in particular [54]. Using the constraint equations from Table 1, the six angles between HD and TH and between TH and PV were finally converted into the model's joint angles $\theta_1$ to $\theta_{39}$.

### 3.3. Joint Torque Estimation

To execute the inverse dynamics calculations, a high-end personal computer with a 2.66 GHz processor was used. For a dataset with 500 samples (5-second trial), the computations took approximately 60 seconds for the Newton-Euler, 690 seconds for the Lagrangian, and 5 seconds for the SimMechanics implementation (based on fourteen executions each).

Fig. 3 depicts the average inverse dynamics input time series for a 315º anterior-left diagonal perturbation during sitting (means ± 1 standard deviations from 5 trials). Shown are the perturbation force and the flexion-extension (FE), lateral bending (LB), and axial rotation (RT) angles of the head (HD) and thorax (TH). Fig. 4 depicts the average FE and LB torques (RT torques within ± 1 Nm) as identified with the input time series and the inverse dynamics routines. Outputs from the three different inverse dynamics methods are plotted on top of each other. The dashed gray lines mark the predictions for the highest cervical and lumbar joints (HD-C2 and TH-L1), whereas the dashed black lines mark the predictions for the lowest cervical and lumbar joints (C7-TH and L5-PV). All other torques are shown using solid gray lines. In the third subplot of Fig. 4 (lumbar FE torques), the thick solid trace outlines the average electromyography of the right erector spinae (at T9; rectified and low-pass-filtered; inverted and not to scale – see [33] for methodological details), demonstrating the involvement of active mechanisms in the balance stabilization act. A sampling-based sensitivity analysis finally revealed that the dynamic model and the inverse dynamics implementations are robust against variations in the geometric and mass-inertia parameters (Appendix C).

A simple visual inspection of Fig. 4 suggests that the joint torque estimates for the Newton-Euler, Lagrangian, and SimMechanics implementations coincide. As this observation was supported by a coefficient of determination ($R^2$) of 99.99 % (standard deviation << 0.01 %) for all forty trials and different time intervals, the internal validity of the inverse dynamics routines is confirmed.

## 4. DISCUSSION AND CONCLUSIONS

The present study takes advantage of the Visible Human Project to identify a detailed three-dimensional dynamic model of the upper body that focuses on the action of the lumbar and cervical spine. The developed model is particularly useful as it (1) is flexible regarding the kinematic nature of the cervical and lumbar joints (free, constrained, or fixed); (2) incorporates all geometric and mass-inertia parameters from a single, high-resolution source; and (3) can be feasibly implemented via different inverse dynamics formulations. Thus, this work directly responds to the postulation that structurally more complex and biologically more realistic models are needed to increase the accuracy of inverse dynamics computations [55]. In what follows, we elaborate on the model's characteristics, but also discuss the three different inverse dynamics routines and the perturbed sitting application.

### 4.1. Model Characteristics

***Joint Kinematics:*** The proposed model has been developed for a particular constellation of six DOF and thirty-three CT (*see Section 2.1.*) that accounts for the intervertebral ranges of motion reported by White and Panjabi [35]. However, because the dynamics have been derived for thirty-nine DOF, other DOF-CT combinations can be easily realized. In other words, the model gives the highest possible degree of flexibility with respect to the assignment of the joint kinematics. For example, particular directions of rotation can be set to zero to (re)produce joint torques for planar applications [14,31,39] or movements without axial rotation [5,32]. Other scenarios may require a fixed cervical spine [5,32], a smaller number of trunk segments [2], or a dynamic model with no constraints at all [18].

***Geometric and Mass-Inertia Parameters:*** A dynamic model is only as good as the geometric and mass-inertia parameters defining it [36]. Even small deviations from the true parameter values can lead to substantial errors in the output measures such as body kinematics or joint torques [10,56]. Consequently, it is highly recommended to utilize parameters that are accurate and based on a single source. However, researchers have been required to implement parameters from multiple sources (e.g., [5,32]), which could potentially compromise the obtained results. One unique feature of the proposed dynamic model is the fact that all geometric and mass-inertia parameters were derived from a single source, i.e., the Male Visible Human, which is public domain [42]. Moreover, the parameters are based on images with a resolution that is more than 1000 times higher than of images used in previous reports on upper body segment parameters (e.g., [57]). Naturally, geometric and mass-inertia parameters can be scaled [58] or used from other sources to reflect different subject anthropometrics.

***Complete Dynamic Description:*** One common assumption of existing dynamic models is to treat them as quasi-static and neglect velocity terms in the equations of motion [29,31,59]. While this assumption simplifies the models and reduces computational efforts, it considerably limits the range of applications or generates undesirable systematic errors in the output measures. To address this limitation, the proposed dynamic model was designed to consider *all* components that contribute to the dynamics of the system. Since the ever-increasing computer power of recent years has made the implementation and simulation of more realistic and complex three-dimensional models possible [7], there is no need anymore to compromise between accuracy, applicability, and complexity. In fact, our inverse dynamics application demonstrates that estimating the joint torques for a dynamic model with thirty-nine DOF is feasible even when considering the velocity terms in the dynamic equations (*see Section 3.3.*).

***Limitations:*** The thoracic spine of the dynamic model was assumed to be rigid based on the report that it is more static during trunk motion [40]. In addition, our perturbation experiments revealed that the three-dimensional trunk angles during perturbed sitting did not significantly differ when measured at two different thoracic locations (around T3 and T7). Nevertheless, we do acknowledge that thoracic rotations likely occur during functional movements of the upper body.

The parameters of the developed model are based on a single cadaver. While obtaining parameters for different subject anthropometrics (e.g., via regression equations) is very beneficial, this was not the objective of the present study. Instead, the Visible Human Project database represented the ideal resource for identifying a complete set of parameters for the use in the developed dynamic model. The model in combination with the parameters will be very useful for investigating emerging scientific questions in biomechanics, neurophysiology, and rehabilitation engineering that require a single, detailed, and accurate 3D dynamic model.

### 4.2. Inverse Dynamics Application

The perturbed sitting application demonstrates that the spinal joint torques can be easily identified using the developed inverse dynamics routines. In addition, since the three formulations were internally validated ($R^2$ of over 99.99999 % for different time intervals), researchers have different options for identifying spinal joint torques. While all routines can be feasibly implemented, each of them has its own advantages. For example, the Newton-Euler formulation is not only comparably efficient, but also identifies the constraint forces between segments as needed for estimating spinal loading during various movements and tasks [2,17-21]. While executing the Lagrangian formulation numerically is comparably complex and, hence, more time-consuming [44], it has the advantage of producing the system's kinetic and potential energies. Finally, the SimMechanics implementation represents more of a 'black box' approach, but is highly efficient and allows the user to quickly alternate between forward and inverse dynamics applications.

The joint torque predictions shown in Fig. 4 may offer various insights into the biomechanical mechanisms of perturbed sitting, but also into balance control efforts that may contribute to re-stabilization. While the head and thorax generally rotate in opposite directions following the anterior-left perturbation (for both FE and LB; Fig. 3), the torque traces for the lumbar and cervical spine exhibit more dissimilar profiles. On the one hand, the *lumbar* torque series are characterized by a steep torque increase component and a flatter torque decrease component (for both FE and LB). As the first component counteracts the torque due to the perturbation and due to increased gravitational forces after body excursion, it basically prevents complete loss of balance. The second component occurs at the end of the perturbation and drives the system back to equilibrium by exceeding the gravitational torques. On the other hand, the *cervical* torque series are characterized by a bimodal profile (for both FE and LB) that primarily results from the opposite displacements of head and thorax (Fig. 3): The first component (FE: +; LB: –) is required to counteract the head displacement itself, whereas the second component (FE: –; LB: +) 'decelerates' the head back to equilibrium under the influence of the trunk kinematics.

In addition to revealing the torque profiles during perturbed sitting, the example shows that the anterior-posterior curvature of the spine has a distinct effect on the lumbar FE torques during body stabilization. In fact, the static upright posture requires lumbar FE torques of different sign (third subplot in Fig. 4, before 0 seconds) – a property that is dependent on the anterior-posterior location of each segment's center of mass and joint center. Moreover, the intersecting of the lumbar FE torque traces (third subplot in Fig. 4, just after 0.2 seconds and at 1.0 seconds) implies that the lower joints do not necessarily carry larger loads, but that the relative magnitudes depend on the actual trunk kinematics. These are important kinetic observations that are masked in trunk models ignoring the spinal curvature [2,5,32].

As the electromyography trace of the right erector spinae indicates (third subplot of Fig. 4), active control components must play a significant role in body re-stabilization. While the electromyography profile has a very similar shape as the joint torque of TH-L1 (which is closest to the electromyography recording site, i.e., T9), the time between the two peaks is approximately 80 ms. This lag agrees with previous reports indicating that the presumably second-order process from muscle activation to force or torque generation takes between 40 and 120 ms [58]. However, since joint reaction torques can be observed even prior to the automatic postural response of the right erector spinae (in agreement with [60]), also passive mechanisms must contribute to the stabilization act. These include spinal stiffness [35-37], viscoelastic properties of the trunk [38], and intra-abdominal pressure [38,39]. Note that the particular contribution of active and passive control mechanisms will be investigated in a future study that uses the developed model in combination with experimental data from a representative group of subjects.

## ACKNOWLEDGMENT

The authors thank Vivian Sin for her assistance in data acquisition and processing. This work was supported by the Canadian Institutes of Health Research (#86427, #94018, and #97953), the Natural Sciences and Engineering Research Council of Canada, the CIHR-STIHR Fellowship in Health Care, Technology and Place (HCTP) (TGF-53911), the University of Toronto, and the Toronto Rehabilitation Institute.

## CONFLICT OF INTEREST STATEMENT

There are no conflicts of interest for the authors of this study.

## LIST OF ABBREVIATIONS

| | |
|---|---|
| $\{F_{SEG}\}$ | Local reference frame of segment |
| $\{F_{WD}\}$ | World reference frame |
| $a_i$ | Length of link i |
| $d_i$ | Offset between links i-1 and i |
| $\alpha_i$ | Twist angle between joints i and i+1 |
| $\theta_i$ | Joint angle between links i-1 and i |
| CT | Constraint |
| DOF | Degree of freedom |
| FE | Flexion-extension |
| HD | Head |
| $J_{6 \times n}$ | Jacobian matrix |
| L | Lagrangian |
| LB | Lateral bending |
| PV | Pelvis |
| $R^2$ | Coefficient of determination |
| RT | Axial rotation |
| T | Kinetic energy |
| $T_{i-1,i}$ | Transformation matrix from frame i-1 to i |
| TH | Thorax |
| V | Gravitational potential energy |

## REFERENCES


[1] Goel VJ, Weinstein JN. ‘Biomechanics of the spine: clinical and surgical perspective’. CRC Press, Boca Raton, Florida, 1990, Chap. 6.

[2] Gagnon D, Larivière C, Loisel P. Comparative ability of EMG, optimization, and hybrid modelling approaches to predict trunk muscle forces and lumbar spine loading during dynamic sagittal plane lifting. Clinical Biomechanics 2001;16:359–372.

[3] Buchanan TS, Lloyd DG, Manal K, Besier TF. Neuromusculoskeletal modeling: estimation of muscle forces and joint moments and movements from measurements of neural command. Journal of Applied Biomechanics 2004;20:367–395.

[4] Sun LW, Lee RYW, Lu W, Luk KDK. Modelling and simulation of the intervertebral movements of the lumbar spine using an inverse kinematic algorithm. Medical and Biological Engineering and Computing 2004;42:740–746.

[5] Wilkenfeld AJ, Audu ML, Triolo RJ. Feasibility of functional electrical stimulation for control of seated posture after spinal cord injury: a simulation study. Journal of Rehabilitation Research and Development 2006;43(2):139–152.

[6] Kim JY, Mills JK, Vette AH, Popovic MR. Optimal combination of minimum degrees of freedom to be actuated in the lower limbs to facilitate arm-free paraplegic standing. ASME Journal of Biomechanical Engineering 2007;129:838–847.

[7] Pandy MG. Computer modeling and simulation of human movement. Annual Review of Biomedical Engineering 2001;3:245–273.

[8] Nakamura Y, Yamane K, Murai A. Macroscopic modeling and identification of the human neuromuscular network. Proceedings of the 28th IEEE EMBS Annual International Conference 2006:99-105.

[9] Murai A, Kurosaki K, Yamane K, Nakamura Y. Musculoskeletal-see-through mirror: Computational modeling and algorithm for whole-body muscle activity visualization in real time. Progress in biophysics and molecular biology 2010;103(2-3):310-317.

[10] Hansen L, de Zee M, Rasmussen J, Andersen TB, Wong C, Simonsen EB. Anatomy and biomechanics of the back muscles in the lumbar spine with reference to biomechanical modeling. Spine 2006;31(17):1888–1899.

[11] Bogduk N, Macintosh JE, Pearcy MJ. A universal model of the lumbar back muscles in the upright position. Spine 1992;17(8):897–913.

[12] Orne D, Liu YK. A mathematical model of spinal response to impact. Journal of Biomechanics 1971;4:49–71.

[13] Liu YK, von Rosenberg DU. The effects of caudocephalad (+Gz) acceleration on the initially curved human spine. Computers in Biology and Medicine 1974;4:85–106.

[14] Crisco JJ 3rd, Panjabi MM. The intersegmental and multisegmental muscles of the lumbar spine. A biomechanical model comparing lateral stabilizing potential. Spine 1991;16(7):793–799.

[15] Shirazi-Adl A, Parnianpour M. Nonlinear response analysis of the human ligamentous lumbar spine in compression. On mechanisms affecting the postural stability. Spine 1993;18(1):147–158.

[16] Granata KP, Wilson SE. Trunk posture and spinal stability. Clinical Biomechanics 2001;16(8):650–659.

[17] McGill SM, Norman RW. Effects of an anatomically detailed erector spinae model on L4/L5 disc compression and shear. Journal of Biomechanics 1987;20(6):591–600.

[18] Jäger M, Luttman A, Laurig W. Lumbar load during one-handed bricklaying. International Journal of Industrial Ergonomics 1991;8:261–277.

[19] McGill SM. A myoelectrically based dynamic three-dimensional model to predict loads on lumbar spine tissues during lateral bending. Journal of Biomechanics 1992;25(4):395–414.

[20] Granata KP, Marras WS. An EMG-assisted model of loads on the lumbar spine during asymmetric trunk extensions. Journal of Biomechanics 1993;26(12):1429–1438.

[21] Granata KP, Marras WS. An EMG-assisted model of trunk loading during free-dynamic lifting. Journal of Biomechanics 1995;28(11):1309–1317.

[22] Daggfeldt K, Thorstensson A. The mechanics of back-extensor torque production about the lumbar spine. Journal of Biomechanics 2003;36(6):815–825.

[23] Nicholas SC, Doxey-Gasway DD, Paloski WH. A link-segment model of upright human posture for analysis of head-trunk coordination. Journal of Vestibular Research 1998;8:187–200.

[24] Fard MA, Ishihara T, Inooka H. Dynamics of the head-neck complex in response to the trunk horizontal vibration: modeling and identification. ASME Journal of Biomechanical Engineering 2003;125:533–539.

[25] Keshner EA. Head-trunk coordination during linear anterior-posterior translations. Journal of Neurophysiology 2003;89:1891–1901.

[26] Schneider K, Zernicke RF, Clark G. Modeling of jaw-head-neck dynamics during whiplash. Journal of Dental Research 1989;68(9):1360–1365.

[27] Garcia T, Ravani B. A biomechanical evaluation of whiplash using a multi-body dynamic model. ASME Journal of Biomechanical Engineering 2003;125:254–265.

[28] Panjabi MM, Pearson AM, Ito S, Ivancic PC, Wang JL. Cervical spine curvature during simulated whiplash. Clinical Biomechanics 2004;19:1–9.

[29] Cholewicki J, McGill SM. Mechanical stability of the in vivo lumbar spine: implications for injury and chronic low back pain. Clinical Biomechanics 1996;11(1):1–15.

[30] Marras WS. The future of research in understanding and controlling work-related low back disorders. Ergonomics 2005;48(5):464–477.

[31] Vanoncini M, Holderbaum W, Andrews B. Development and experimental identification of a biomechanical model of the trunk for functional electrical stimulation control in paraplegia. Neuromodulation 2008;11(4):315–324.

[32] Lambrecht JM, Audu ML, Triolo RJ, Kirsch RF. Musculoskeletal model of trunk and hips for development of seated-posture-control neuroprosthesis. Journal of Rehabilitation Research and Development 2009;46(4):515–528.

[33] Masani K, Sin V, Vette AH, Thrasher TA, Kawashima N, Morris A, Preuss R, Popovic MR. Postural reactions of the trunk muscles to multi-directional perturbations in sitting. Clinical Biomechanics 2009;24(2):176–182.

[34] Thrasher TA, Sin VW, Masani K, Vette AH, Craven BC, Popovic MR. Responses of the trunk to multidirectional perturbations during unsupported sitting. Journal of Applied Biomechanics 2010;26(3):332–340.

[35] White AA, Panjabi MM. 'Clinical biomechanics of the spine', 2nd edition. Lippincott Williams & Wilkins, Philadelphia, Pennsylvania, 1990, Chaps. 1-2.

[36] Panjabi MM, Brand RA, White AA. Three-dimensional flexibility and stiffness properties of the human thoracic spine. Journal of Biomechanics 1976;9:185–192.

[37] Gardner-Morse MG, Stokes IAF. Structural behavior of human lumbar spinal motion segments. Journal of Biomechanics 2004;37:205–212.

[38] Gardner-Morse MG, Stokes IAF. Trunk stiffness increases with steady-state effort. Journal of Biomechanics 2001;34:457–463.

[39] Cholewicki J, Juluru K, McGill SM. Intra-abdominal pressure mechanism for stabilizing the lumbar spine. Journal of Biomechanics 1999;32:13–17.

[40] Preuss R, Fung J. Musculature and biomechanics of the trunk in the maintenance of upright posture. Journal of Electromyography and Kinesiology 2008;18(5):815–828.

[41] Denavit J, Hartenberg RS. A kinematic notation for low-pair mechanisms based on matrices. ASME Journal of Applied Mechanics 1955;23:215–221.

[42] Vette AH, Yoshida T, Thrasher TA, Masani K, Popovic MR. A complete, non-lumped, and verifiable set of upper body segment parameters for three-dimensional dynamic modeling. Medical Engineering and Physics 2011;33(1):70-79.

[43] Kim JY. '3D dynamic modeling, control synthesis, and controllability analysis for FES-assisted paraplegic standing'. M.A.Sc. thesis, University of Toronto, Canada, 2005.

[44] Hollerbach JM. A recursive Lagrangian formulation of manipulator dynamics and a comparative study of dynamics formulation complexity. IEEE Transactions on Systems, Man, and Cybernetics 1980;10(11):730–736.

[45] Vette AH, Sanin E, Bulsen A, Morris A, Masani K, Popovic MR. A portable and automated postural perturbation system for balance assessment, training, and neuromuscular system identification. ASME Journal of Medical Devices 2008;2(4):041007-1 to 041007-9.

[46] Angeloni C, Cappozzo A, Catani F, Leardini A. Quantification of relative displacement of skin- and plate-mounted markers with respect to bones. Journal of Biomechanics 1993;26:864.

[47] Karlsson D, Tranberg R. On skin movement artifact: resonant frequencies of skin markers attached to the leg. Human Movement Science 1999;18:627–635.

[48] Manal K, McClay I, Stanhope S, Richards J, Galinat B. Comparison of surface mounted markers and attachment methods in estimating tibial rotations during walking. Gait and Posture 2000;11:38–45.

[49] Gilles M, Wing AM, Kirker SG. Lateral balance organisation in human stance in response to a random or predictable perturbation. Experimental Brain Research 1999;124(2):137–144.

[50] Robertson DGE, Caldwell GE, Hamill J, Kamen G, Whittlesey SN. 'Research methods in biomechanics'. Human Kinetics, Champaign, Illinois, 2004, Chap. 2.

[51] Craig JJ. ‘Introduction to robotics – mechanics and control’, 3rd edition. Addison-Wesley, New York City, New York, 2004, Chaps. 2, 5 & 6.

[52] Areblad M, Nigg BM, Ekstrand J, Olsson KO, Ekstrom H. Three-dimensional measurements of rearfoot motion during running. Journal of Biomechanics 1990;23:933–940.

[53] Cole GK, Nigg BM, Ronsky JL, Yeadon MR. Application of the joint coordinate system to three-dimensional joint attitude and movement representation: a standardization proposal. ASME Journal of Biomechanical Engineering 1993;115:344–349.

[54] Crawford NR, Yamaguchi GT, Dickman CA. Methods for determining spinal flexion/extension, lateral bending, and axial rotation from marker coordinate data: analysis and refinement. Human Movement Science 1996;15:55–78.

[55] Hatze H. The fundamental problem of myoskeletal inverse dynamics and its implications. Journal of Biomechanics 2002;35:109–115.

[56] Jensen RK. Human morphology: its role in the mechanics of movement. Journal of Biomechanics 1993;26(Suppl. 1):81–94.

[57] Pearsall DJ, Reid JG, Livingston LA. Segmental inertial parameters of the human trunk as determined from computed tomography. Annals of Biomedical Engineering 1996;24:198–210.

[58] Winter DA. ‘Biomechanics and motor control of human movement’. John Wiley & Sons, New Jersey City, New Jersey, 2005, Chap. 3.

[59] Gardner-Morse MG, Stokes IAF, Laible JP. The role of muscles in stability of the lumbar spine. Journal of Orthopaedic Research 1995;13:802–808.

[60] Weerdesteyn V, Laing AC, Robinovitch SN. Automated postural responses are modified in a functional manner by instruction. Experimental Brain Research 2008;186:571–580.

[61] Driels MR, Fan UJ, Pathre US. The application of Newton-Euler recursive methods to the derivation of closed form dynamic equations. Journal of Robotic Systems 1988;5(3):229–248.

[62] Asada H, Slotine JJE. ‘Robot analysis and control’. Wiley, New York City, New York, 1986, Chaps. 3 & 5.

[63] Wood GD, Kennedy DC. Simulating mechanical systems in Simulink with SimMechanics, 2003: http://www.mathworks.com/matlabcentral/fx_files/2871/1/SimMechanics.pdf (June 20, 2010).

[64] Kiemel T, Elahi AJ, Jeka JJ. Identification of the plant for upright stance in humans: multiple movement patterns from a single neural strategy. Journal of Neurophysiology 2008;100:3394–3406.

[65] Vette AH, Masani K, Nakazawa K, Popovic MR. Neural-mechanical feedback control scheme generates physiological ankle torque fluctuation during quiet stance. IEEE Transactions on Neural Systems and Rehabilitation Engineering 2010;18(1):86–95.

[66] Vette AH, Masani K, Kim JY, Popovic MR. Closed-loop control of functional electrical stimulation-assisted arm-free standing in individuals with spinal cord injury: a feasibility study. Neuromodulation 2009;12(1):22–32.

[67] Kim JY, Popovic MR, Mills JK. Dynamic modeling and torque estimation of FES-assisted arm-free standing for paraplegics. IEEE Transactions on Neural Systems and Rehabilitation Engineering 2006;14(1):46–54.

# APPENDIX A – INVERSE DYNAMICS IMPLEMENTATION

## A1. Newton-Euler Implementation

The Newton-Euler formulation was implemented as a series of equations that consisted of two sequential components: forward and backward computation [51,61]. For each point in time, the forward computation calculated the instantaneous segment velocities and accelerations, as well as the inertia forces and moments at each segment's center of mass. Once the forward computation had been completed, the backward computation identified the constraint forces and intervertebral joint torques [61].

In order to account for the effect of external perturbations, the Newton-Euler implementation needed to translate the external forces from the point of application to the joint above the perturbed segment. For the purpose of simplification, the reference frame assigned to the point of application was chosen to have the same orientation as the first frame at the superior joint. The translated forces were then added to the joint forces in the backward computation [61].

## A2. Lagrangian Implementation

Unlike the Newton-Euler formulation, the Lagrangian formulation does not identify the joint torques via the constraint forces and torques. Instead, it uses the partial derivatives of the Lagrangian ($L$), which is defined as the difference between the sum of all kinetic energies ($T$) and the sum of all gravitational potential energies ($V$) of the links [51,62]. The partial differentiation is, however, time consuming for an open-loop chain with many degrees of freedom (DOF), which can make the model implementation inefficient or even unfeasible. To resolve this issue, we decided to obtain the general symbolic expressions of the partially differentiated Lagrangian rather than a unique equation for each joint variable.

For body kinematics in the absence of external forces, the joint torque $\tau_i$ is then given by:

$$\tau_i = \frac{d}{d\,t}\left(\frac{\partial L}{\partial \dot{q}_i}\right) - \frac{\partial L}{\partial q_i} \;. \tag{A1}$$

Also,

$$\begin{gathered}\frac{\partial L}{\partial q_i} = \frac{\partial T_i}{\partial q_i} + \frac{\partial T_{i+1}}{\partial q_i} + \cdots + \frac{\partial T_j}{\partial q_i} + \cdots + \frac{\partial T_{39}}{\partial q_i} - \frac{\partial V_i}{\partial q_i} - \frac{\partial V_{i+1}}{\partial q_i} - \cdots - \frac{\partial V_j}{\partial q_i} - \cdots - \frac{\partial V_{39}}{\partial q_i} \\ \frac{\partial L}{\partial \dot{q}_i} = \frac{\partial T_i}{\partial \dot{q}_i} + \frac{\partial T_{i+1}}{\partial \dot{q}_i} + \cdots + \frac{\partial T_j}{\partial \dot{q}_i} + \cdots + \frac{\partial T_{39}}{\partial \dot{q}_i},\end{gathered} \tag{A2}$$

where $i$ denotes the $i$-th revolute joint, $q_i$ the angle of the $i$-th joint, and $j$ the $j$-th link. According to Eq. (A2), the partial derivative of a given link's kinetic or potential energy can be non-zero for $i \le j$. For these cases, we obtained the general symbolic expressions of the partially differentiated Lagrangian, i.e., $\frac{\partial L}{\partial q_i}$ and $\frac{\partial L}{\partial \dot{q}_i}$, and quantified them by substituting the constants and variables with respective numerical values. Calculating the time derivative of $\frac{\partial L}{\partial \dot{q}_i}$ using the central difference scheme finally allowed us to obtain the joint torques [62].

To account for perturbations, the external forces underwent the same translation as for the Newton-Euler formulation (*see Appendix A1*). The equation for calculating the joint torque $\tau_i$ then changes to:

$$\tau_i = \frac{d}{d\,t}\left(\frac{\partial L}{\partial \dot{q}_i}\right) - \frac{\partial L}{\partial q_i} - \left[{}^0J^T \;\; {}^0F_{ext}\right]_i . \tag{A3}$$

For the calculation of this particular Jacobian ${}^0J^T$, the segment experiencing the external forces ${}^0F_{ext}$ was treated as the last link of the system. Consequently, the Jacobian's size depends on where the external forces are applied: if they act on the *n*-th link of the model, ${}^{0}J^{T}$ in Eq. (A3) has the dimension of $n \times 6$. The effects of the forces are summed in case multiple segments are perturbed [62].

### A3. SimMechanics Implementation

Using the Simulink and SimMechanics blocksets in Matlab, the model of the upper body was implemented as a series of user-defined rigid bodies and revolute joints. At a given intervertebral joint, the three rotational DOF (flexion-extension, lateral bending, and axial rotation) were represented by three revolute joint blocks with one DOF each. These joints were consecutively linked to three body blocks. The first two blocks were mass- and dimensionless, and the last block exhibited the inertial and geometric properties of the given body segment. This procedure was repeated for all thirteen segments of the upper body model.

To execute the inverse dynamics simulations, each revolute joint was attached to a joint actuator block (for generating rotation) and a joint sensor block (for calculating joint torques). In addition, body actuator blocks were linked to the body blocks to implement external forces (i.e., perturbations). For mathematical details on the dynamic routines used in SimMechanics, the reader should consult the work by Wood and Kennedy [63].

## APPENDIX B – SINGULARITY ANALYSIS FOR CLOSED-LOOP CONTROL

Neuromuscular mechanisms of postural control are often studied via dynamic models that are implemented in closed-loop control schemes [64,65]. Such closed-loop model studies are also needed to investigate the feasibility of developing a neuroprosthesis for sitting and standing balance, and to identify adequate control strategies [33,34,66]. If dynamic models with six DOF are used for these applications, the knowledge of singularities is very important: At a singular configuration, at least one direction exists in the task space in which the system is not able to translate or rotate, regardless of the selected joint velocities. This also implies that the joint velocities required to maintain a desired motion near singular configurations may become extremely large. Consequently, singular configurations and their immediate neighborhoods should be avoided.

Singularities are identified by studying the system's Jacobian matrix (*see also Appendix A2*), which transforms the joint space velocities into task space velocities [51,62]. For the proposed dynamic model of the upper body, the Jacobian matrix $J_{6\times39}$ can be reduced to a 6 × 6 Jacobian matrix $J^*_{6\times6}$ (transformation of the joint velocities $\dot{\theta}_1$ to $\dot{\theta}_3$ and $\dot{\theta}_{19}$ to $\dot{\theta}_{21}$ into task space velocities) using the constraint equations from Table 1. Joint angle combinations at which $J^*_{6\times6}$ loses its full rank finally indicate distinct singularities in the task space.

The examination of $J^*_{6\times6}$ was performed numerically [67]. For this purpose, a six-dimensional space of joint angles was identified using kinematic data from the subject that was perturbed in eight different horizontal directions. $J^*_{6\times6}$ was examined not only for these experimental joint angle combinations, but also for a cloud of six-dimensional joint angles that was limited by the maximum/minimum joint angles observed in the experiments (spacing of five degrees, resulting in approximately $4 \bullet 10^6$ joint angle combinations). Since $J^*_{6\times6}$ did not lose full rank for any of the examined joint angle combinations based on the default tolerance of the Matlab command 'rank' (see Matlab documentation for details), no singularities were detected.

## APPENDIX C – PARAMETER SENSITIVITY ANALYSIS

To assess whether the dynamic model and the inverse dynamics implementations are robust against variations in the geometric and mass-inertia parameters, a basic sensitivity analysis was performed. The following parameters were either systematically or randomly varied: (1) segment masses; (2) segment inertia tensors; (3) spinal joint coordinates; and (4) center of mass coordinates. As the segment masses and inertias are correlated with each other ('mass-inertia parameters'), respective parameters were varied in parallel. For the same reason, also the joint and center of mass coordinates ('geometric parameters') were varied in parallel. As shown in Table 3, ten different parameter sets were used: for the first eight sets, the parameters for all the segments/joints were varied by the indicated factor; for the last two sets, the parameters were changed randomly across the segments/joints by either -10, 0, or +10 %.

Fig. 5 exemplifies the effect of the parameter variation on the calculated torques for the lowest cervical and lumbar joints (C7-TH and L5-PV). Shown are the flexion-extension (FE) as well as the lateral bending (LB) torques for the original parameters (solid black lines) and the most extreme variations (sets 5 and 8 in Table 3; dashed gray lines). Outputs from the three different inverse dynamics methods are again plotted on top of each other ($R^2$=99.99 %). It can be seen in Fig. 5 that the torque profiles are similar for the three parameter sets, but that an increase (decrease) in the parameters will generally result in an increase (decrease) of the calculated torque peaks. This can be explained by the fact that increasing the masses (inertias, joint distances, COM distances) will result in larger torques that are needed to overcome gravitational and/or inertia forces.

Table 3 shows the C7-TH and L5-PV torque peaks for all 10 parameter sets, expressed as ratios with respect to the original torque peaks. The largest (smallest) torque peaks where found when the magnitude of all parameters was increased (decreased) by 10 % (extreme sets 5 and 8,

Fig. 5). In addition, it can be seen that varying the geometric parameters had a larger effect on the torque peaks than varying the mass-inertia parameters (sets 1 to 4). As the overall results agree with the findings presented in Fig. 5 and Table 3, the sensitivity analysis suggests that both the model and the implementation of the inverse dynamics routines are robust.

## TABLE LEGENDS

**Table 1.** Constraint equations for all CT and all directions of motion (FE: flexion-extension, RT: axial rotation, LB: lateral bending). The equations are based on the ranges of motion of the vertebral joints as reported by White and Panjabi [35].

**Table 2.** Link parameters of the kinematic model following the Standard Denavit-Hartenberg formulation as applied in the frame assignment depicted in Figure 2. $a_i$ are the constant link lengths, $d_i$ the constant link offsets, $\alpha_i$ the constant twist angles, and $q_i$ the time-varying revolute joint angles.

**Table 3.** Results of the sampling-based sensitivity analysis. Model parameters were increased/decreased by 10 %; calculated torque peaks at the lowest cervical and lumbar joints (C7-TH, L5-PV) were expressed as ratios with respect to the original torque peaks (FE: flexion-extension, LB: lateral bending).

## FIGURE LEGENDS

**Fig. 1.** Schematic representation of the geometric model of the upper body. The model had a total of six revolute degrees of freedom (DOF) and thirty-three revolute constraints (CT) that were located at the centers of thirteen intervertebral discs (three DOF or CT per joint). The C7-TH and L5-PV joints were DOF-joints. The remaining joints were constrained to the motion of the subjacent DOF-joints according to the ranges of motion given by White and Panjabi [35].

**Fig. 2.** Frame assignment to (A) the lumbar spine and (B) the cervical spine using the Standard Denavit-Hartenberg notation. The last frame $\{F_{39}\}$ was assigned to the vertex of the head, whereas the inertial coordinate frame $\{F_0\}$ represented a fixed translation of the world frame $\{F_{WD}\}$ to the L5-PV joint.

**Fig. 3.** Inverse dynamics input time series for a 315° anterior-left diagonal perturbation during sitting. Shown are the perturbation force and the FE, LB, and RT angles of HD and TH. Solid black lines mark the means, and dashed gray lines mark the standard deviations of the time series (five trials). The vertical line across the subplots indicates the onset of the perturbation.

**Fig. 4.** Inverse dynamics output time series for a 315° anterior-left diagonal perturbation during sitting. Shown are the FE and LB torques from the three inverse dynamics methods (plotted on top of each other). The dashed gray lines mark the predictions for the highest cervical and lumbar joints (HD-C2 and TH-L1), whereas the dashed black lines mark the predictions for the lowest cervical and lumbar joints (C7-TH and L5-PV). The torques at the other nine joints are marked by solid gray lines. The vertical line across the subplots indicates the onset of the perturbation, and the thick solid line in the third subplot outlines the average electromyography of the right erector spinae (at T9).

**Fig. 5.** Effect of parameter variation on the the calculated torques for the lowest cervical and lumbar joints (C7-TH and L5-PV). Shown are the flexion-extension (FE) as well as the lateral bending (LB) torques for the original parameters (solid black lines) and for the 'extreme' parameter sets 5 and 8 in Table 3 (dashed gray lines). Outputs from the three different inverse dynamics methods are plotted on top of each other.

**Table 1.** Constraint equations for all CT and all directions of motion (FE: flexion-extension, RT: axial rotation, LB: lateral bending). The equations are based on the ranges of motion of the vertebral joints as reported by White and Panjabi [35].

| Joint | FE | RT | LB |
|---|---|---|---|
| **L5-PV** | $\theta_1$ | $\theta_2$ | $\theta_3$ |
| **L4-L5** | $\theta_4 = \frac{16}{17}\theta_1$ | $\theta_5 = 2\,\theta_2$ | $\theta_6 = 2\,\theta_3$ |
| **L3-L4** | $\theta_7 = \frac{15}{17}\theta_1$ | $\theta_8 = 2\,\theta_2$ | $\theta_9 = \frac{8}{3}\theta_3$ |
| **L2-L3** | $\theta_{10} = \frac{14}{17}\theta_1$ | $\theta_{11} = 2\,\theta_2$ | $\theta_{12} = 2\,\theta_3$ |
| **L1-L2** | $\theta_{13} = \frac{12}{17}\theta_1$ | $\theta_{14} = 2\,\theta_2$ | $\theta_{15} = 2\,\theta_3$ |
| **TH-L1** | $\theta_{16} = \frac{12}{17}\theta_1$ | $\theta_{17} = 2\,\theta_2$ | $\theta_{18} = \frac{8}{3}\theta_3$ |
| **C7-TH** | $\theta_{19}$ | $\theta_{20}$ | $\theta_{21}$ |
| **C6-C7** | $\theta_{22} = \frac{17}{9}\theta_{19}$ | $\theta_{23} = 3\,\theta_{20}$ | $\theta_{24} = \frac{7}{4}\theta_{21}$ |
| **C5-C6** | $\theta_{25} = \frac{20}{9}\theta_{19}$ | $\theta_{26} = \frac{7}{2}\theta_{20}$ | $\theta_{27} = 2\,\theta_{21}$ |
| **C4-C5** | $\theta_{28} = \frac{20}{9}\theta_{19}$ | $\theta_{29} = \frac{7}{2}\theta_{20}$ | $\theta_{30} = \frac{11}{4}\theta_{21}$ |
| **C3-C4** | $\theta_{31} = \frac{15}{9}\theta_{19}$ | $\theta_{32} = \frac{7}{2}\theta_{20}$ | $\theta_{33} = \frac{11}{4}\theta_{21}$ |
| **C2-C3** | $\theta_{34} = \frac{10}{9}\theta_{19}$ | $\theta_{35} = \frac{3}{2}\theta_{20}$ | $\theta_{36} = \frac{10}{4}\theta_{21}$ |
| **HD-C2** | $\theta_{37} = \frac{20}{9}\theta_{19}$ | $\theta_{38} = 20\,\theta_{20}$ | $\theta_{39} = \frac{5}{4}\theta_{21}$ |

**Table 2.** Link parameters of the kinematic model following the Standard Denavit-Hartenberg formulation as applied in the frame assignment depicted in Figure 2. $a_i$ are the constant link lengths, $d_i$ the constant link offsets, $\alpha_i$ the constant twist angles, and $q_i$ the time-varying revolute joint angles.

| **Joint axis ($i$ = 1…39)** | $a_i$ **[mm]** | $d_i$ **[mm]** | $\alpha_i$ **[deg]** | $q_i$ **[deg]** | **Motion** |
|---|---|---|---|---|---|
| **3** | 39.054 | 3.249 | 90 | $90 + \theta_3$ | **L5-PV** |
| **6** | 38.913 | -4.886 | 90 | $90 + \theta_6$ | **L4-L5** |
| **9** | 38.780 | -8.878 | 90 | $90 + \theta_9$ | **L3-L4** |
| **12** | 35.755 | -11.932 | 90 | $90 + \theta_{12}$ | **L2-L3** |
| **15** | 35.808 | -9.704 | 90 | $90 + \theta_{15}$ | **L1-L2** |
| **18** | 295.772 | 17.049 | 90 | $90 + \theta_{18}$ | **TH-L1** |
| **21** | 18.239 | 9.527 | 90 | $90 + \theta_{21}$ | **C7-TH** |
| **24** | 17.106 | 4.907 | 90 | $90 + \theta_{24}$ | **C6-C7** |
| **27** | 18.067 | 1.552 | 90 | $90 + \theta_{27}$ | **C5-C6** |
| **30** | 18.051 | -0.213 | 90 | $90 + \theta_{30}$ | **C4-C5** |
| **33** | 19.096 | 1.616 | 90 | $90 + \theta_{33}$ | **C3-C4** |
| **36** | 20.039 | 0.948 | 90 | $90 + \theta_{36}$ | **C2-C3** |
| **39** | 172.656 | -5.801 | 90 | $90 + \theta_{39}$ | **HD-C2** |
| **all other** | 0 | 0 | 90 | $90 + \theta_i$ | **-** |

**Table 3.** Results of the sampling-based sensitivity analysis. Model parameters were increased/decreased by 10 %; calculated torque peaks at the lowest cervical and lumbar joints (C7-TH, L5-PV) were expressed as ratios with respect to the original torque peaks (FE: flexion-extension, LB: lateral bending).

| Set | Δ mass-inertia | Δ geometric | C7-TH torque peak | | L5-PV torque peak | |
|---|---|---|---|---|---|---|
| | | | FE | LB | FE | LB |
| **1** | +10 % | 0 % | 1.132 | 1.137 | 1.105 | 1.112 |
| **2** | 0 % | +10 % | 1.152 | 1.160 | 1.121 | 1.129 |
| **3** | -10 % | 0 % | 0.904 | 0.887 | 0.928 | 0.912 |
| **4** | 0 % | -10 % | 0.879 | 0.872 | 0.908 | 0.899 |
| **5** | +10 % | +10 % | 1.270 | 1.287 | 1.227 | 1.238 |
| **6** | +10 % | -10 % | 0.941 | 0.929 | 0.950 | 0.959 |
| **7** | -10 % | +10 % | 1.039 | 1.053 | 1.035 | 1.025 |
| **8** | -10 % | -10 % | 0.770 | 0.760 | 0.829 | 0.797 |
| **9** | random 1a | random 1b | 0.892 | 0.899 | 0.925 | 0.944 |
| **10** | random 2a | random 2b | 1.107 | 1.099 | 1.063 | 1.063 |

Figure 1
Click here to download high resolution image

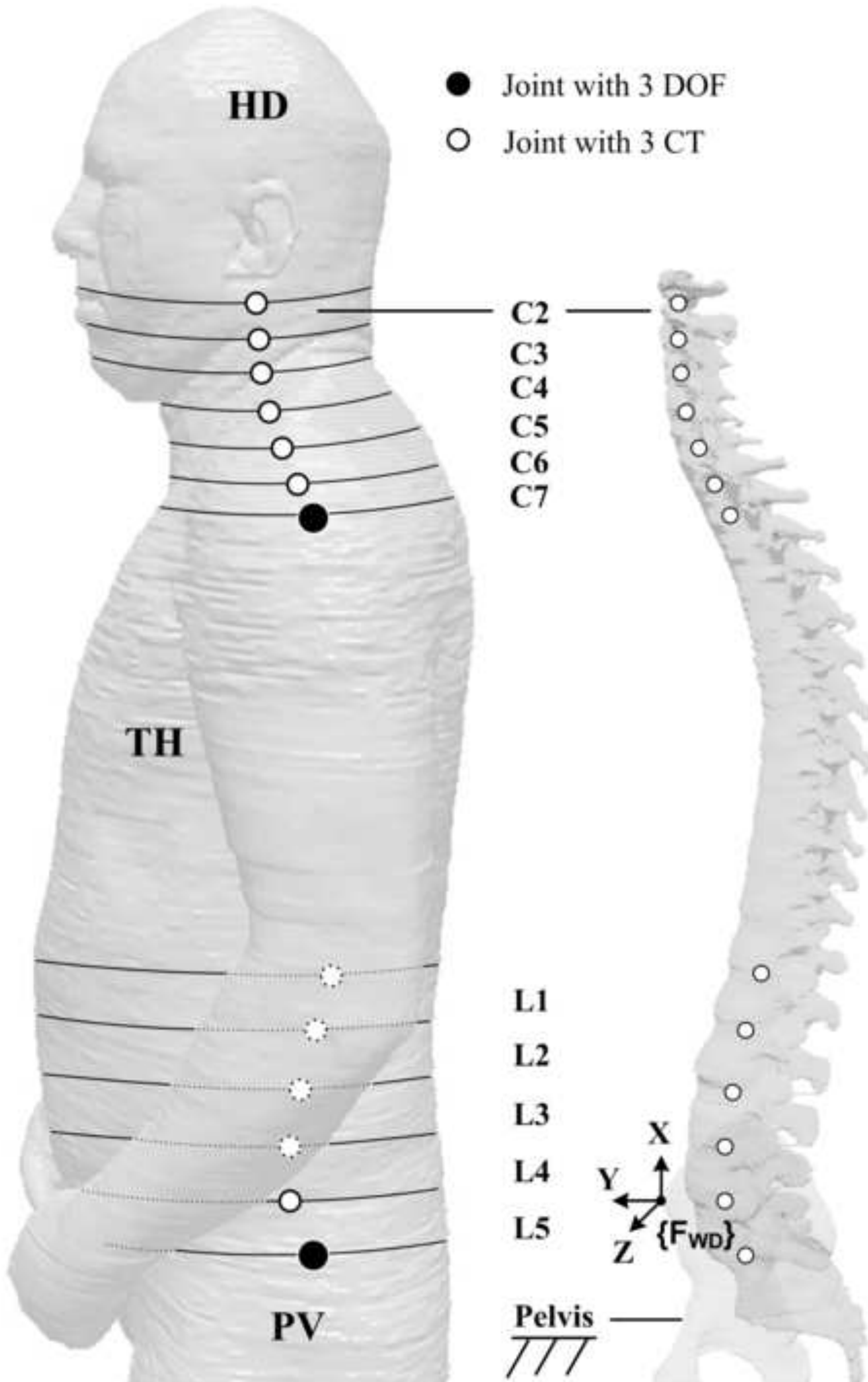

Figure 2
Click here to download high resolution image

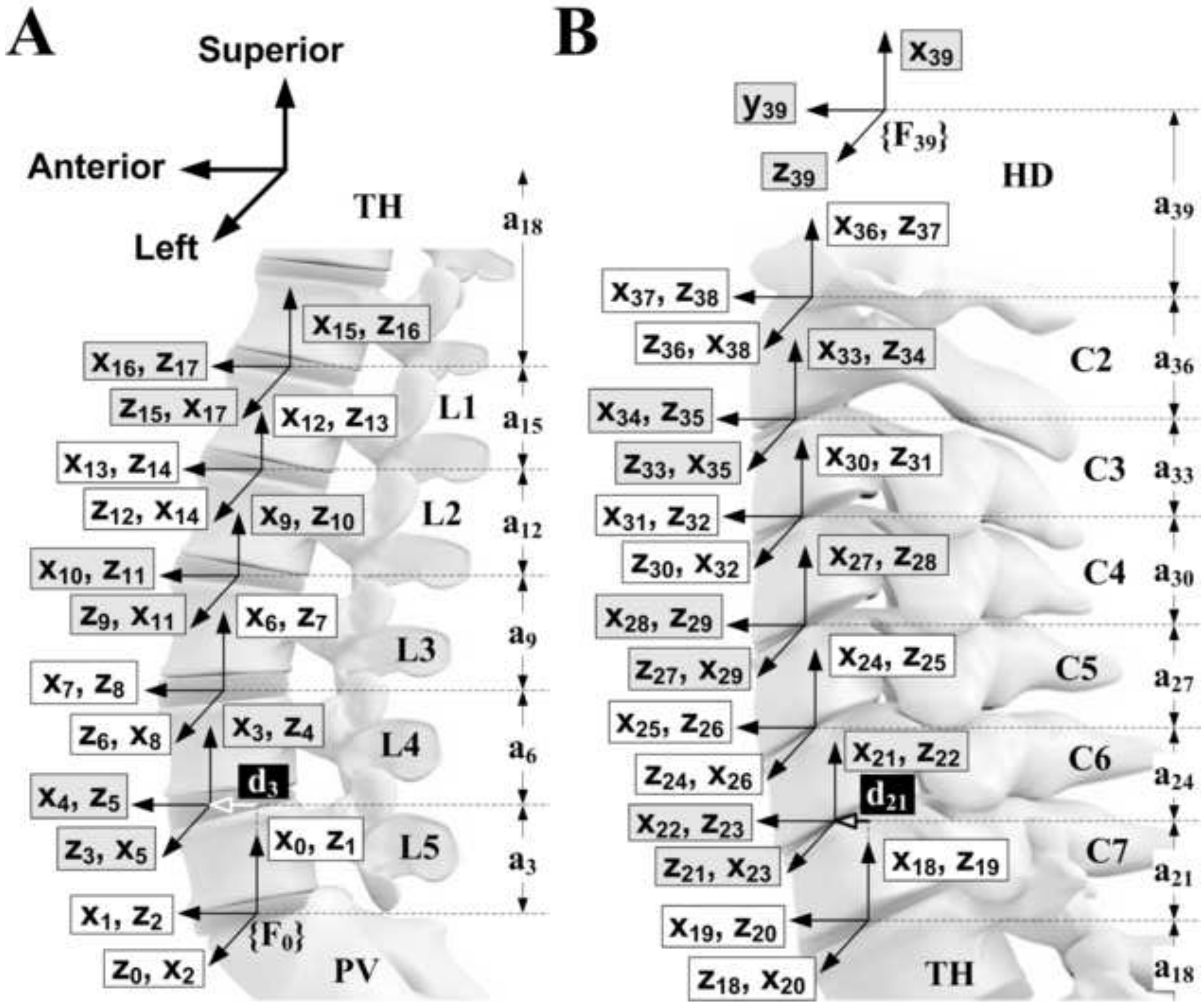

Figure 3
Click here to download high resolution image

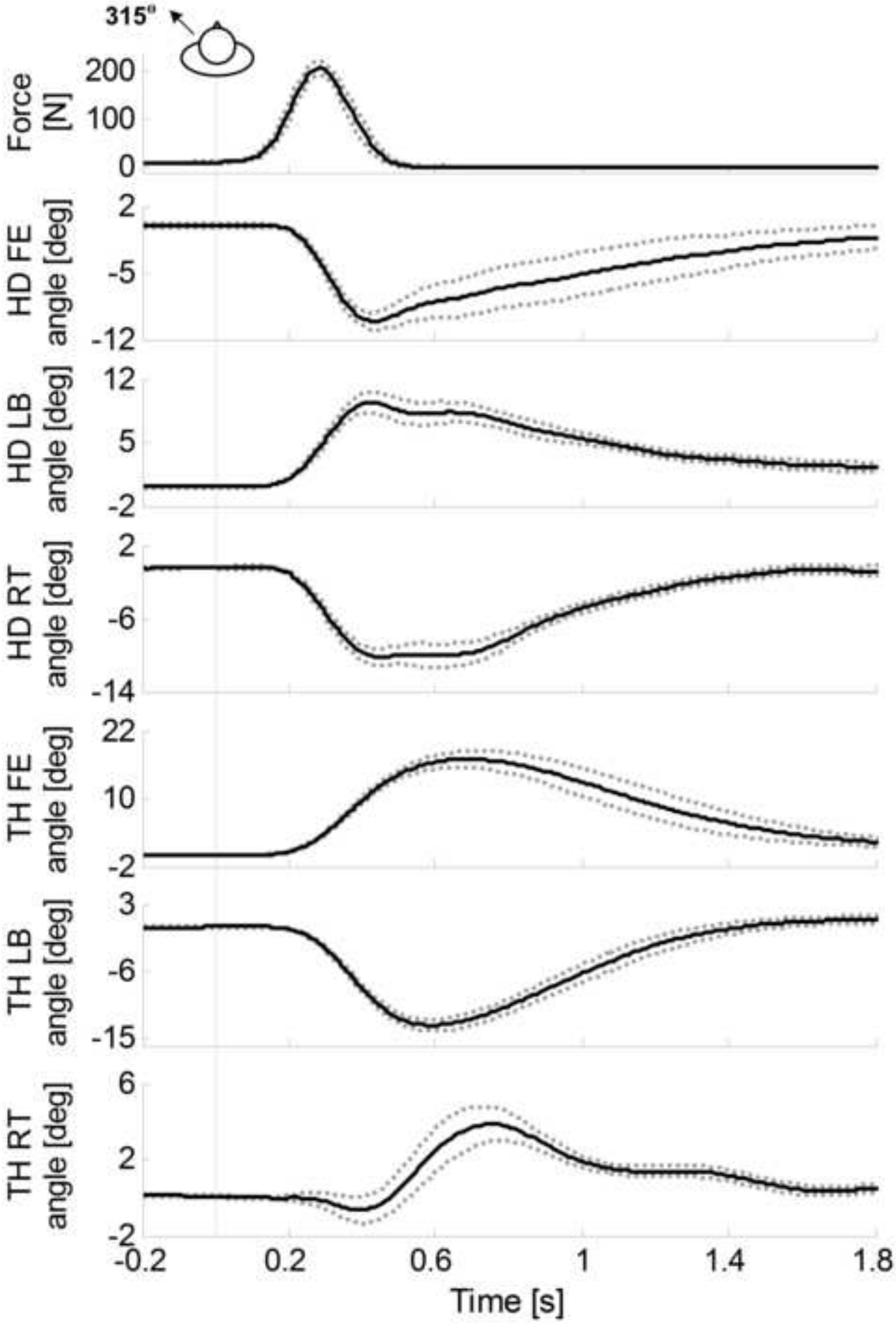

Figure 4
Click here to download high resolution image

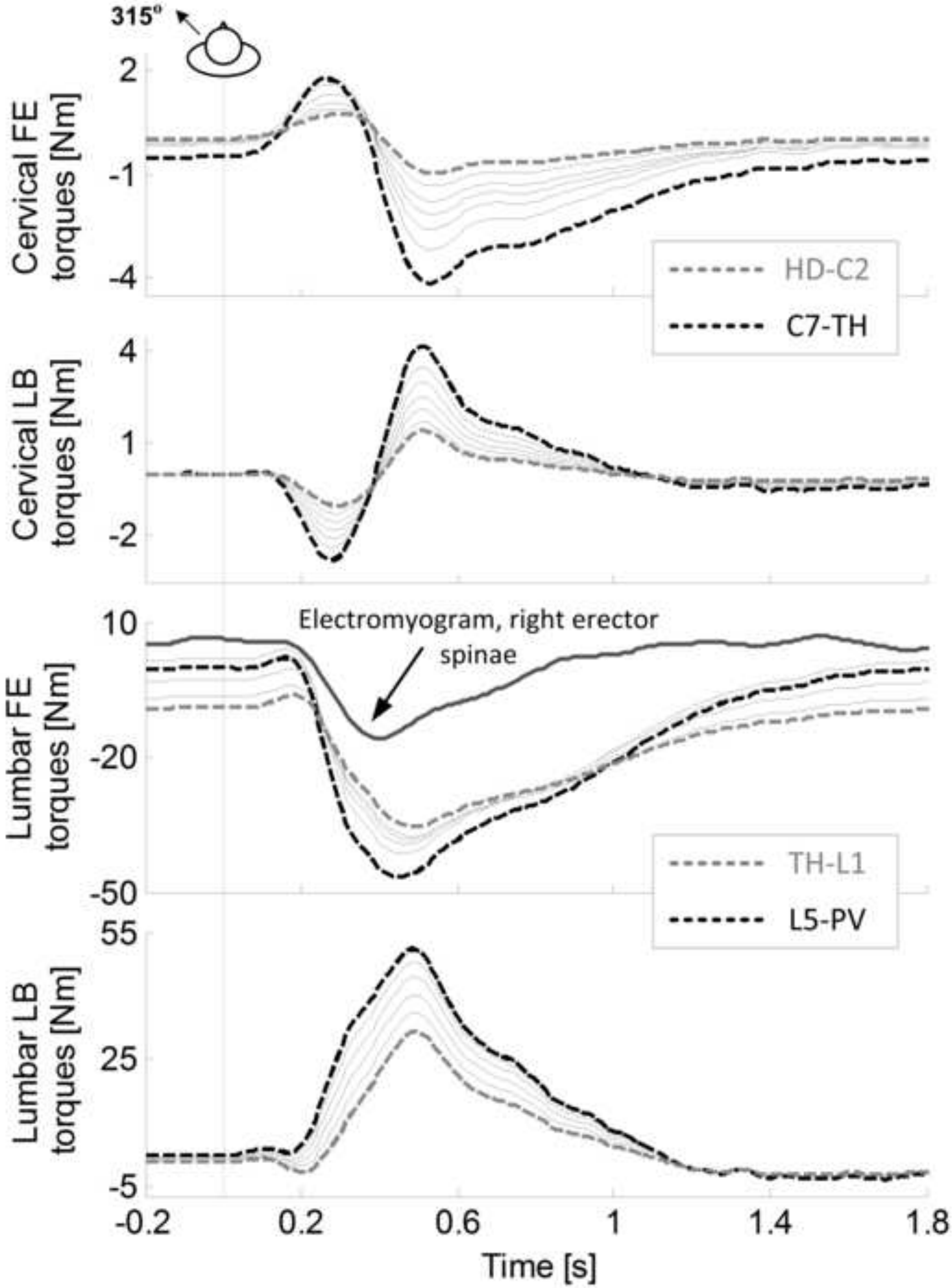

Figure 5
Click here to download high resolution image